PRECISION
RAMAN

Best-in-class Raman microscopes
for research and analytical requirements
backed with world-class customer
support and service.

edinst.com

RESEARCH ARTICLE

Journal of RAMAN SPECTROSCOPY WILEY

Identification of iron compounds in chrysotile from the Balangero mine (Turin, Italy) by micro-Raman spectroscopy

Laura Fornasini[1] | Simona Raneri[1] | Danilo Bersani[2] |
Luciana Mantovani[3] | Valentina Scognamiglio[4] | Dario Di Giuseppe[4] |
Alessandro F. Gualtieri[4]

[1]ICCOM-CNR, Institute of Chemistry of Organometallic Compounds, National Research Council, Pisa, Italy

[2]Department of Mathematical, Physical and Computer Sciences, University of Parma, Parma, Italy

[3]Department of Chemistry, Life Sciences and Environmental Sustainability, University of Parma, Parma, Italy

[4]Department of Chemical and Geological Sciences, University of Modena and Reggio Emilia, Modena, Italy

Correspondence
Laura Fornasini, ICCOM-CNR, Institute of Chemistry of Organometallic Compounds, National Research Council, Via G. Moruzzi 1, Pisa 56124, Italy.
Email: laura.fornasini@pi.iccom.cnr.it

Abstract

Chrysotile, one of the six regulated asbestos minerals, is classified as carcinogenic to humans by the International Agency for Research on Cancer. The Balangero mine (Turin, Italy) was the largest asbestos mine in Europe, providing extraction of chrysotile fibers until 1990. Chrysotile from Balangero is currently of great interest in fibers toxicity studies focused on the understanding of the mechanisms that induce lung malignancies. One of the crucial factors in the biochemical reactions is the presence of Fe at the fibers surface. Surface reactivity is responsible for the generation of reactive oxygen species, which play an important role in asbestos cyto-genotoxicity. Moreover, the dissolution of Fe-bearing phases in the acidic environment of the lysosomes might be considered as possible release of hazardous Fe ions in the lungs. Here, chrysotile from Balangero was characterized by micro-Raman spectroscopy and scanning electron microscope-energy dispersive system (SEM-EDS) analysis to identify the Fe-bearing impurities associated with asbestos fibers. Micrometric crystals were recognized as Fe oxides, carbonates, and sulfides. Uncommonly reported phases in asbestos minerals were also identified, mainly as mackinawite (Fe (II)S), in different forms. The nature of the Fe compounds containing both Fe(II) and Fe(III) species was verified by micro-Raman spectroscopy combined with SEM-EDS analysis.

KEYWORDS
asbestos, chrysotile, iron compounds, micro-Raman spectroscopy, SEM-EDS

1 | INTRODUCTION

The term *asbestos*, used both with a commercial and regulatory relevance, refers to a group of six naturally occurring hydrated silicates with a fibrous-asbestiform habit.[1,2] The group includes amphibole asbestos (actinolite asbestos, amosite, anthophyllite asbestos, crocidolite, and tremolite asbestos) and serpentine asbestos

(chrysotile).[1,2] Thanks to their outstanding technological properties such as flexibility, thermal, and chemical resistance, asbestos minerals have been extensively exploited and traded from the mid-19th century and during the 20th century.[1,2] Industrial applications as building materials ranged from compact materials (i.e., asbestos-cement products, pipes and water tanks, chimney tops, and floor tiles) to friable asbestos (i.e., insulating panels, household products, and artificial ashes).[3,4] As of today, asbestos was banned in more than 60 countries worldwide, and other nations put restrictions on its use.[5] The six asbestos minerals were classified as carcinogenic to humans and regulated by the International Agency of Research on Cancer (IARC).[1] Inhalation of asbestos fibers is strictly associated with the development of lung diseases, such as lung cancer, malignant mesothelioma, and asbestosis.[1] Asbestos-related diseases are still a health issue, considering its current use in many countries including China, India, and Russia and the occurrence of asbestos containing materials—still present—in buildings.[5,6] Ongoing toxicological research is focused on investigating the pathogenic mechanisms, which induce human diseases, not well understood yet. The morphology of the fibers (e.g. crystal habit, length and width), together with their surface activity and biopersistence, are key parameters in toxicity/pathogenicity of asbestos.[1,2,7] Furthermore, the occurrence of trace metals in the crystal structure may play a crucial role in the surface reactivity, inducing metals release during the dissolution of the fibers in the organic environment.[7] Specifically, the Fe content needs to be considered in asbestos fibers, being present both as a constitutive component of mineral fibers (as in crocidolite and amosite) and as a substituent for another ion (as for Mg^{2+} in chrysotile).[7] By reducing molecular O_2, Fe catalyzes the formation of toxic reactive oxygen species (ROS)—following the Haber–Weiss reactions—leading to DNA damage, protein oxidation, and lipid peroxidation.[8–11] Several *in vitro* and *in vivo* studies highlighted the key role of Fe in the mechanisms of asbestos toxicity.[7,11–13] However, the mechanisms involved in Fe mobilization and utilization by macrophages are still not fully understood.[12–15]

Chrysotile, as one of the serpentine polymorphs together with antigorite and lizardite, is a layer silicate made of Si-centered tetrahedral (T) and Mg-centered octahedral (O) sheets with the ideal chemical formula $Mg_3(OH)_4Si_2O_5$.[2,16,17] Its cylindrical structure, consisting in the rolling of the TO layer around the fiber axis, results from the misfit between the T and the O sheets and due to the polarity of the TO unit.[16,17] Substitutions may occur with the replacement of Al^{3+} for Si^{4+} or Mg^{2+} in the T and O sheets, respectively; Fe^{2+} and Fe^{3+} may also substitute Mg^{2+} in the O sheet,[8,17,18] and Fe^{3+} may occasionally replace Si^{4+} in the T sheet.[17,19] Trace metals (such as Cr, Ni, Co, Mn, and Cu) are also intimately associated with chrysotile, as naturally present in the raw material due to the geochemical processes involved in its formation.[7,20] As in the case of Fe^{2+}, metal impurities are usually isomorphous substituent for Mg^{2+} in the O sheet.[7] Concerning the chrysotile toxicity, Fe and metal releases are strictly connected to that of Mg, when the fibers are dissolved in an acidic environment.[7] In detail, the acidic environment that characterizes the phagocytosis process induces the chrysotile fibers dissolution and the release of metals (e.g., Fe, Mn, Cr, and Ni).[7] When released into lung tissues, these metals may prompt ROS, which plays an active role in inducing pulmonary diseases.[7,21,22]

In chrysotile, the amount of Fe may range from ∼1% up to ∼5%.[18,19,23,24] In addition to the structural Fe, Fe-bearing compounds are often found within chrysotile samples, related to their formation processes.[18,19,25,26] Usually, the most abundant Fe compound is magnetite (Fe_3O_4), formed during the serpentinization processes.[25,27] Fe and Ni sulfides (pentlandite, heazlewoodite, pyrrhotite, troilite, and others) and Fe-Ni alloys are also generally found in serpentinized peridotites.[26–28]

Chrysotile is the most employed asbestos mineral, having been mined in more than 95% of the commercially developed asbestos ore deposits.[6,29] In Western Europe, the largest asbestos mine is located in Balangero, in the Western Alps near Turin (Italy), where chrysotile was extracted until 1990.[6,30] Chrysotile from Balangero is currently of great interest in the evaluation of airborne and waterborne asbestos fibers in the proximity of the abandoned mine.[31–33] To date, the toxicity of chrysotile fibers from Balangero was deeply examined, and in vitro studies are currently in progress in inspecting the acute effects of this carcinogenic mineral.[7,34–36] Chrysotile asbestos from Balangero belongs to the Balangero serpentinite of the Lanzo Ultramafic Massif,[26] has a typical crystal-chemical formula $(Mg_{5.81}Fe^{2+}_{0.15}Al_{0.27}Fe^{3+}_{0.09}Cr_{0.01})_{6.33}(OH)_{7.11}Si_{3.97}O_{10}$,[25] and forms bundles of flexible fibrils with splayed ends.[37,38] Pollastri and coworkers[39] found that Fe is mainly substituent for Mg in the octahedral sites, with possible minor tetrahedral Fe. Furthermore, Fe is a constitutive component in balangeroite, a fibrous inosilicate with a gageite-like structure and chemical formula $(Mg,Fe^{2+},Fe^{3+},Mn^{2+})_{42}O_6[Si_4O_{12}]_4(OH)_{40}$, which occasionally intergrows with chrysotile from Balangero, accounting for 0.2–1 wt% of the chrysotile extracted.[26,40–42] Although balangeroite is not considered an asbestos mineral, it is noteworthy that balangeroite fibers in chrysotile asbestos might slightly contribute

to the overall toxicity of the fibers from Balangero, though cannot be considered responsible for the widespread diffusion of mesothelioma in patients exposed to asbestos fibers in the area of Balangero.[42,43] In addition to balangeroite, other mineralogical phases were detected in Balangero chrysotile as impurities (<1 wt%), namely, antigorite, calcite, clinochlore, diopside, dolomite, magnetite, microcline, plagioclase, and talc.[25] Currently, Balangero chrysotile is often used in *in vitro* studies to investigate the toxicity of asbestos, including the acute inflammatory effects.[36,44] Detecting and recognizing these impurities, especially Fe-bearing compounds, in chrysotile asbestos employed in toxicological studies could be relevant in understanding its toxicity and the mechanisms involved in Fe mobilization in chrysotile.

In the present work, we report the Raman characterization of the chrysotile fibers and the intergrown fibrous/lamellar species found in chrysotile asbestos from Balangero. In fact, micro-Raman spectroscopy was successfully employed to identify asbestiform minerals and to detect other minor phases found with the fibers, even at the trace level.[45–50] Fe-bearing impurities were identified in micrometric crystals by micro-Raman spectroscopy. Morphological and chemical investigation of the mineral particles was performed using a scanning electron microscope (SEM) equipped with an energy dispersive system (EDS). Raman spectroscopy enables the identification of several Fe compounds at trace level, which were not detected with other analytical techniques (i.e. optical microscopy, X-ray powder diffractometry) in previous studies,[25,26] due to their occurrence under the detection limit. Some of these species are uncommonly reported in association with asbestos minerals.[28] In chrysotile from Balangero, the presence of Fe (II) and Fe (III), both as structural element of the fibers – i.e. chrysotile and balangeroite – and as minor component – i.e. in Fe compounds – should be considered as possible metal release in the reactivity and dissolution of asbestos fibers in the lungs.

2 | MATERIALS AND METHODS

The sample consists of raw chrysotile from the abandoned asbestos mine of Balangero (45°17′37″ N, 7°30′25″ E) near Turin, Italy. The fibrous powdered sample (Figure S1, Supporting Information) was prepared for the micro-Raman analysis in a sealed configuration, working in a fume hood: a small amount of powder (≤ 1 mg) was sticked to a double-sided tape adhering on a microscope glass. The powder was covered by a coverslip and sealed to the glass substrate. Three copies were prepared and analyzed to ensure a good statistical data acquisition.

Micro-Raman measurements were performed with two spectrometers, using different laser lines as excitation wavelengths. A He-Ne 632.8 nm and a frequency doubled Nd:YAG 473.1 nm laser lines were used with a Horiba Jobin Yvon LabRam (HORIBA Scientific, Kyoto, Japan) confocal micro-spectrometer (300 mm focal length), equipped with an integrated Olympus BX40 microscope (Olympus, Tokyo, Japan) with 4x, 10x, 50x ULWD and 100x objectives, an 1800 grooves/mm grating, a XY motorized stage and a Peltier cooled silicon CCD (1024 × 256 pixels). The spectral resolution is ~2 cm^{-1} with the 632.8 nm line and ~4 cm^{-1} with the 473.1 nm line. Further micro-Raman measurements were acquired with a Horiba Jobin Yvon LabRam HR Evolution (HORIBA Scientific, Kyoto, Japan) confocal micro-spectrometer (800 mm focal length), using a Nd:YAG 532 nm, a He-Ne 632.8 nm and a diode 785 nm laser lines, an integrated Olympus BX41 microscope (Olympus, Tokyo, Japan) with a 5x, 10x, 50x ULWD and 100x objectives, a 600 grooves/mm grating, a XY motorized stage and a liquid nitrogen cooled silicon CCD (1024 × 256 pixels). The confocal hole was fixed at 100 μm. The spectral resolution is ~1 cm^{-1} (785 nm), ~2 cm^{-1} (632.8 nm) and ~3 cm^{-1} (532 nm). The spectra were acquired in different spectral regions from 50 cm^{-1} to 4000 cm^{-1}. The systems were calibrated using the 520.6 cm^{-1} Raman peak of silicon in the low-wavenumber spectral range and using the emission lines of a gas lamp in the high-wavenumber range. In both instruments, density filters were used to reduce the laser power (< 3 mW at the sample), in order to avoid heating effects. The spatial resolution was ~2 μm, using the 50x ULWD objective, which was usually used to better focus on the sample under the coverslip. Typical acquisitions were 30 s repeated at least 4 times. Data analysis was performed with the *LabSpec 5* software. The fluorescence background was removed by subtracting a polynomial curve as baseline. The Raman peaks in the spectra were deconvoluted with Gaussian-Lorentzian curves to determine the contributions of each mineral phase.

SEM-EDS analyses were done using a Jeol 6400 Scanning Electron Microscope equipped with an Oxford EDS microprobe at the University of Parma. Additional analyses were performed using the JSM-6010PLUS/LA SEM equipped with an Oxford INCA-350 EDS spectrometer at the University of Modena and Reggio Emilia. Microprobe analysis operating conditions were 20 kV and 1.2 mA current, ~1 μm beam diameter, and a counting time of about 75 s; the chemical composition is obtained after averaged about 10 analytical points per sample. The powder samples were deposited on a scotch-tape over a glass section and then covered with a high-conductance graphite film to avoid charging effects. To assess the presence

of heterogeneities in chemical composition or discriminate different mineralogical phases, SEM images were obtained using back-scattered electron (BSE), and secondary electron images (SEIs) are taken to identify the morphology of the sample.

3 | RESULTS AND DISCUSSION

Chrysotile from Balangero (Turin, Italy) is a white-grayish fibrous material with darker grains. At the microscope scale, the mineral fibrous content is combined with a minor non-fibrous portion (Figure 1). The mineral fibers consist mainly of bundles of flexible and curvilinear fibers with frayed ends, as typical of the chrysotile morphology.[37]

The Raman spectra acquired from these fibers show the characteristic signals of chrysotile (Figure 2), which
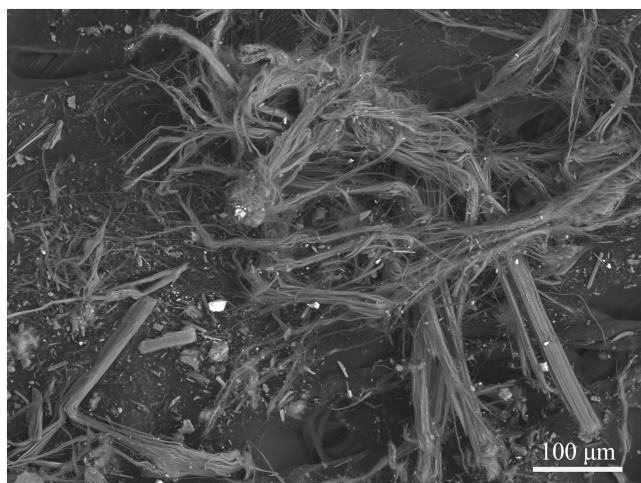

FIGURE 1 Scanning electron microscope back-scattered electron (SEM-BSE) image of chrysotile asbestos from Balangero.
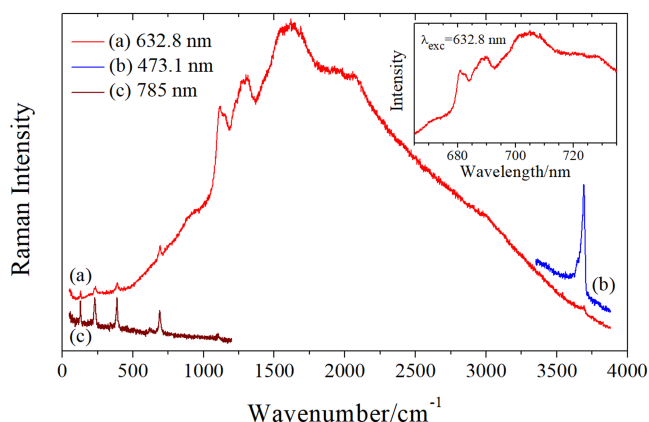
FIGURE 2 Raman spectra of a chrysotile fiber from Balangero obtained at (a) 632.8 nm, (b) 473.1 nm, and (c) 785 nm. In the inset the photoluminescence emissions of Cr^{3+} ions are magnified. [Colour figure can be viewed at wileyonlinelibrary.com]

were recorded with different excitation wavelengths. The spectrum obtained at 632.8 nm (Figure 2a) shows both the Raman signal of the fiber in the low-wavenumber spectral range (50–1200 cm^{-1}) and in the OH stretching range (3500–3800 cm^{-1}). A better signal-to-noise ratio at high wavenumbers is obtained using the 473.1 nm laser line (Figure 2b), considering both the quantum efficiency of the silicon charge-coupled device (CCD) in this range and the ν^4 dependence on the intensity of the scattered radiation. In the low-wavenumber region, the fluorescence contribution can be considerably reduced selecting the 785 nm laser wavelength (Figure 2c). Interestingly, photoluminescence peaks are also visible in the spectrum acquired with the He-Ne excitation. Large bands occurring between 670 and 730 nm (corresponding to the spectral range 900–2100 cm^{-1}) are characteristics of Cr^{3+} and Cr-Cr pairs emissions (inset in Figure 2).[51,52] Solomonov and coworkers[52] observed photoluminescence peaks due to the presence of Cr in antigorite, consisting of Cr^{3+} emission (R line) at 687 nm ($^2E \rightarrow \, ^4A_2$ transition) and Cr-Cr pairs contributions (N lines) from 663 to 724 nm due to the splitting of the ^2E and $^4A_2$ states. Although photoluminescence emissions are sensitive to chemical and structural changes of the local environment of Cr ions, similar emission patterns are expected for antigorite and chrysotile. Cr as trace metal may substitute Mg in the octahedral sites of brucite layer in the chrysotile structure, as well as in antigorite.[16] Previous studies confirmed that chrysotile contains Cr as trace element—together with other metals such as Mn, Ni, and Co.[20,53] Furthermore, its concentration in Balangero chrysotile asbestos is even higher (>1000 ppm) than in other chrysotile samples.[20]

The Raman spectrum of the chrysotile fiber is reported also in Figure 3a,b, after background subtraction. In the low-wavenumber range (Figure 3a), between 100 and 1200 cm^{-1}, the vibrational modes of chrysotile lattice and internal vibrations of the SiO_4 tetrahedra are shown, the main signals occurring at 129, 233, 389, 691, and 1101 cm^{-1}. The univocal identification of chrysotile among the other serpentine polymorphs (antigorite, lizardite, and polygonal serpentine) was confirmed by its typical Raman bands of the OH stretching vibrations, between 3500 and 3800 cm^{-1}. Chrysotile shows the main peak at ~3695 cm^{-1} with a shoulder (~3680 cm^{-1}) and a weaker contribution at ~3647 cm^{-1}, as reported in Figure 3b.[45,54] At a deeper investigation, chrysotile fibers are strictly associated with other accessory mineral species, showing two different morphologies: plate lamellae and rigid fibers are occasionally found within the sample, as shown in the SEM images in Figure 3c,d. Antigorite and balangeroite are present as accessory phases in chrysotile from Balangero. They were observed
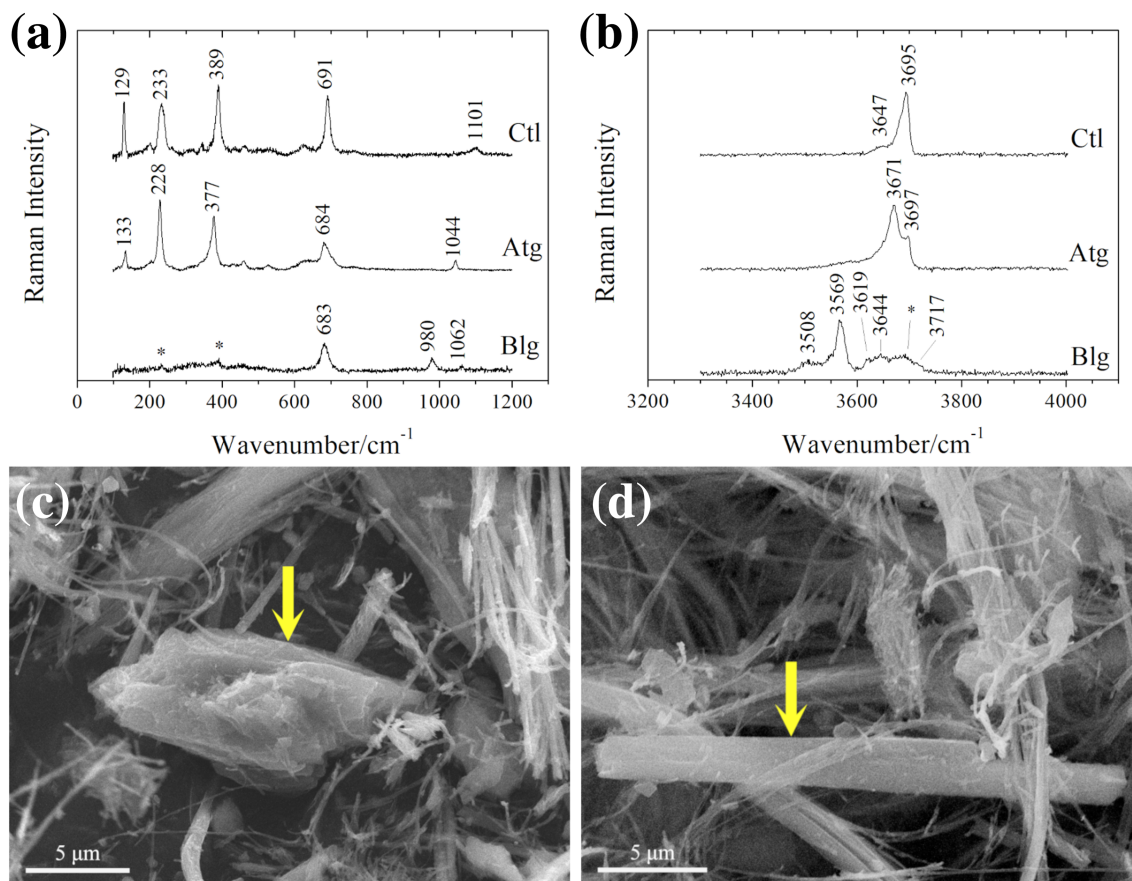
FIGURE 3 (a and b) Raman spectra of chrysotile (Ctl), antigorite (Atg), and balangeroite (Blg) in Balangero chrysotile: (a) in the low-wavenumber region obtained at 785 nm and (b) in the OH stretching spectral range obtained at 473.1 nm. Chrysotile features mixed with other fibers are marked with an asterisk (*). (c and d) Scanning electron microscope secondary electron images (SEM-SEI) of an antigorite lamella and a balangeroite fiber, respectively, highlighted by the yellow arrows. [Colour figure can be viewed at wileyonlinelibrary.com]

intimately intergrown with chrysotile fibers.[25,26,40,55] Here, antigorite and balangeroite are identified by their Raman spectra, respectively (Figure 3a,b). Antigorite occurs as stocky plate particles with a lamellar habit (Figure 3c).[56] In antigorite, low-wavenumber vibrational modes are typically shifted towards lower wavenumbers compared with chrysotile, being at 133, 228, 377, 684, and 1044 cm^{-1} (Figure 3a). In addition, the identification of antigorite was assessed by its characteristic peak at 1044 cm^{-1}, corresponding to the antisymmetric stretching mode of the Si-O$_b$-Si groups. In the OH stretching vibrational range, antigorite shows a doublet with the main peak at 3671 cm^{-1} and a weaker signal at 3697 cm^{-1} (Figure 3b).[45,54] On the other hand, balangeroite is characterized by thin, rigid, and brittle fibers (Figure 3d).[40] In the low-wavenumber region, balangeroite usually shows a less intense Raman signal than chrysotile and antigorite, with its main peak at 683 cm^{-1} and weaker features at 980 and 1062 cm^{-1}. The distinctive OH stretching bands with its strongest peak at 3569 cm^{-1} and other contributions at 3508, 3619, 3644,

and 3717 cm^{-1} confirmed the discrimination of balangeroite among the other fibrous phases.[26,57] Weak features from chrysotile fibers are generally detected together with those of balangeroite, due to their similar structure (as marked with the symbol * in Figure 3a,b). In balangeroite, the presence of Fe as a constitutive element is confirmed by the EDS spectrum (Figure S2). Another asbestiform mineral usually associated with chrysotile fibers and discovered in several serpentinite bodies from the Piemonte Zone, namely, carlosturanite,[26,58,59] was not found in chrysotile from Balangero (this work). Carlosturanite was observed in fractured serpentinites in Varaita, Viù, and Po valleys, while it was not reported near the area of the Balangero mine.[58] Notwithstanding that carlosturanite may be distinguished from serpentine-group minerals and other asbestiform silicates by its characteristic Raman spectrum,[60] the phase might not be detected, if its occurrence is considerably scarce. As a matter of fact, micro-Raman measurements are punctual analyses, each measuring spot being representative of a few microns (~2 μm) of the investigated sample. The

main Raman signals of carlosturanite would have been found at 671, 706, and 776 cm^{-1} in the low-wavenumber spectral range and at 3585 and 3685 cm^{-1} in the OH stretching spectral region.[26,60]

Besides the fibrous content, Balangero chrysotile includes also non-fibrous impurities as micrometric crystals located near and on the surface of the fibers, ranging from few micrometers to ~40 μm. The most abundant compound consists of magnetite (α-Fe$_3$O$_4$) in black crystals, which are found both isolated in the material and attached to mineral fibers, as shown by the SEM images in Figure 4a,b. A typical Raman spectrum acquired on these crystals shows magnetite features at 304, 525, and **665** cm^{-1} (in bold type the strongest peak) (Figure 4c). Because it is well-known that magnetite undergoes a phase oxidation transformation to hematite with increasing temperature, the laser power was reduced to less than 1 mW at the sample during the Raman acquisitions, in order to avoid heating effects.[61,62] EDS spectra (Figure S3) confirm the presence of Fe in the crystals, also reporting Mg and Si signals, due to the composition of the neighboring fibers (Figure 4b) or tiny fiber fragments

on the crystal itself (Figure 4a). Magnetite is known to be widely present in chrysotile asbestos, being formed during the serpentinization processes.[26,63] Other Fe-bearing impurities were identified in Balangero chrysotile through micro-Raman measurements, whose presence is rarer than magnetite crystals. Reddish to black micrometric crystals consist of Fe oxides as ilmenite (FeTiO$_3$) and hematite (α-Fe$_2$O$_3$). Their Raman spectra are shown in Figure 4d, with ilmenite characteristic peaks at 232, 371, and **683** cm^{-1} and hematite features occurring at **226**, 245, **292**, 410, 496, 610, and 660 cm^{-1}.[61,62,64] In addition, an Fe oxyhydroxide was also found, as lepidocrocite (γ-FeO(OH)), with Raman peaks at **247**, 302, **385**, and 528 cm^{-1}.[62] As for the identification of magnetite, a low laser power (<1 mW) was used during the Raman acquisitions. Even in these cases, the Raman signal of the mineral fibers was occasionally recorded along with that of Fe compounds, as reported for lepidocrocite (marked with the symbol * in Figure 4d). Furthermore, for crystals of a few microns size, the signals from surrounding fibers can be unlikely avoided, considering the spatial resolution of the micro-spectrometer configuration (~2 μm).
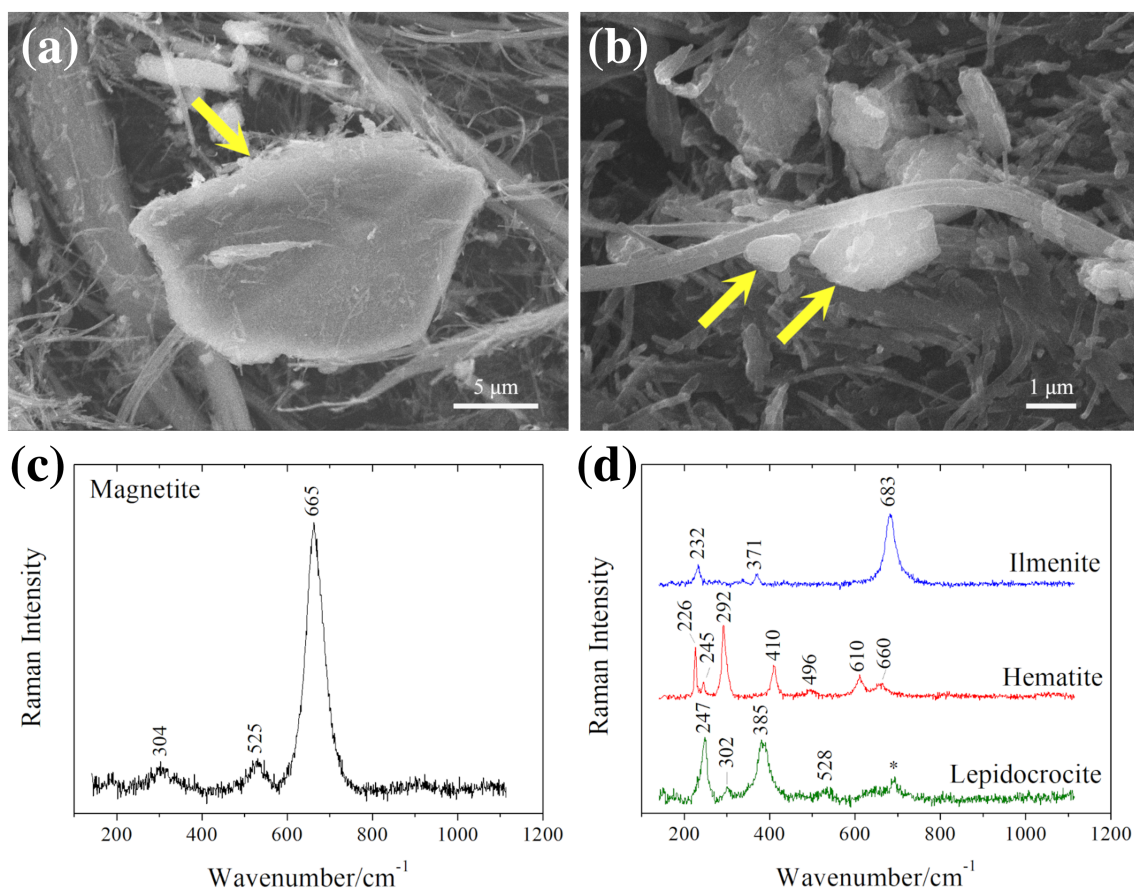
FIGURE 4 (a and b) Scanning electron microscope secondary electron images (SEM-SEI) of magnetite crystals in Balangero chrysotile, highlighted by the yellow arrows; (c) Raman spectrum of a magnetite crystal in Balangero chrysotile; (d) Raman spectra of Fe oxides and oxyhydroxides in Balangero chrysotile: ilmenite, hematite, and lepidocrocite. Weak feature of mineral fibers detected with lepidocrocite signals is marked with an asterisk (*). [Colour figure can be viewed at wileyonlinelibrary.com]

In Balangero chrysotile, Fe-bearing impurities are not restricted to oxides and oxyhydroxides. Micrometric crystals, ranging from pale yellow to reddish color, were identified as carbonates. The Raman spectrum is reported in Figure 5a. The symmetrical stretching vibration of the CO_3^{2-} group occurred at 1057 cm^{-1}. The most intense signal consists of an asymmetrical band at **531** cm^{-1} with a shoulder at ~560 cm^{-1}. Other peaks were found at 142, 283, and 438 cm^{-1}. This carbonate species does not correspond to a univocal carbonate phase, according to the literature.[65–67] However, some minerals belonging to the hydrotalcite group (e.g., stichtite and pyroaurite) show similar Raman spectra. Stichtite peaks were found at 131, 288, 316, 460, 534, 1017, and 1057 cm^{-1}, whereas pyroaurite peaks at 139, 284, 527 and 1058 cm^{-1}.[66,67] The occurrence of a pure Fe carbonate was excluded because the typical features of siderite $FeCO_3$ were not observed.[65] The EDS analysis proved the presence of both Fe and Mg as main elements in the crystal (Figure 5b), suggesting that it is a mixed Fe-Mg carbonate, similar to pyroaurite.[67]

Concerning other Fe compounds, black micrometric crystals were also identified as Fe sulfides, in different forms. Grains of irregular shape were found mixed with the fibrous phases, as isolated crystals or attached to the mineral fibers. A typical Fe sulfide crystal is shown in the SEM image in Figure 6a, whose EDS spectrum reveals the presence of Fe and S as the main elements (Figure S4a). The Raman spectra on these crystals proved the occurrence of various species containing both Fe and S, as reported in Figure 6b. Among them, signals corresponding to different species were found, even combined within the same measuring spot. In details, the Raman spectra of the single species are shown in the curves I and II in Figure 6b. The first one (curve I) consists of two sharp peaks at 204 and **280** cm^{-1}. The most intense peak at 280 cm^{-1} is attributed to the symmetric stretching mode of Fe-S bond, while the weak contribution at 204 cm^{-1} is due to a lattice mode.[68] The Raman spectrum may be attributed to that of nanocrystalline mackinawite (Fe(II) S), according to the literature.[69] The second species (curve II) is distinguished by six Raman peaks at 122, 168,
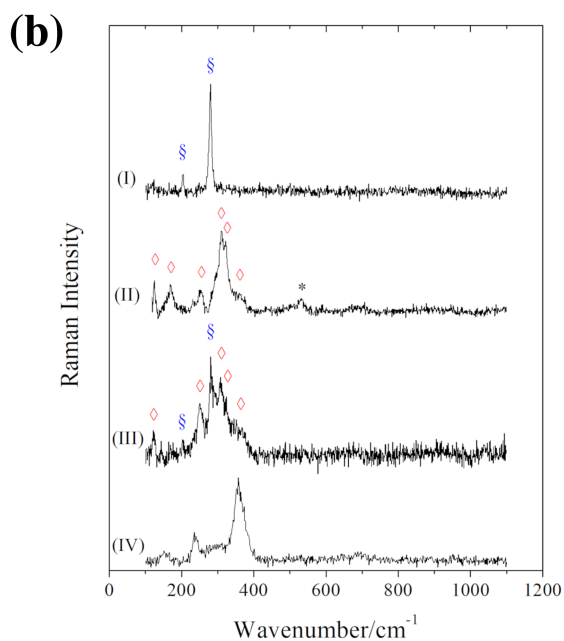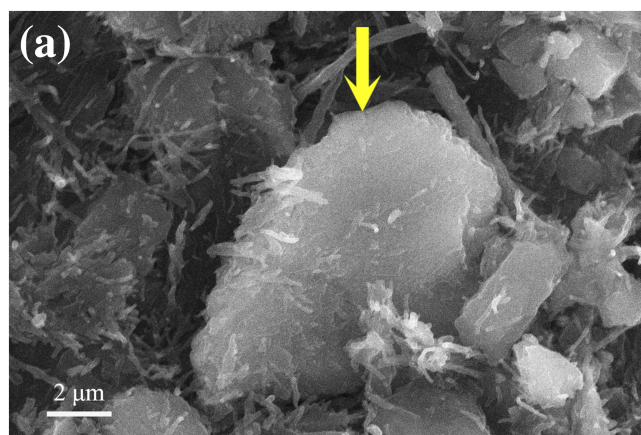
253, **309**, 323, and ~355–360 cm^{-1}. These signals correspond to those detected by Bourdoiseau and coworkers in Fe(III)-containing mackinawite (Fe(II)$_{1-3x}$Fe(III)$_{2x}$S), obtained through the partial oxidation of mackinawite crystals.[69,70] Fe(III) ions partially substitute Fe(II) inside the crystalline structure of mackinawite, with the formation of the so-called partially oxidized mackinawite.[69,70] The features of both species were also recorded together within the same measuring spot, as reported in the spectrum in curve III of Figure 6b. Sometimes, traces of other compounds, such as those of Fe-Mg carbonate, were found mixed with sulfides signals (as marked with the symbol * in curve II in Figure 6b). The presence of mackinawite is uncommonly reported as minor species in asbestos: small irregularly shaped crystals were only observed under an optical microscope by Zucchetti.[28] Mackinawite occurring in different forms may be considered as an intermediate product in the formation process of Fe oxides and oxyhydroxides.[71] It has been reported that mackinawite is sensitive to the oxidizing action of O_2.[71] Partially oxidized mackinawite was described as the first intermediate compound in the transformation of mackinawite into greigite (Fe_3S_4) and then into elemental S and Fe(III) oxyhydroxides and/or magnetite.[70,71] Occasionally, in Balangero, chrysotile another sulfide was found in black micro-crystals, whose Raman spectrum is reported in curve IV of Figure 6b, consisting of an intense band at **359** cm^{-1} and weaker signals at ~151 and 238 cm^{-1}. The EDS spectrum (Figure S4b) reveals the presence of Ni in addition to Fe and S, identifying this species as an Fe-Ni sulfide. According to the existing literature data and Raman database, a precise correspondence with a univocal mineral phase was not found. The EDS analysis suggests that this species may have an intermediate composition between pentlandite ((Fe,Ni)$_9S_8$) and horomanite (Fe$_6$Ni$_3S_8$), highlighting the presence of Ni as toxic metal.

As Fe-based sulfides (pyrite, pyrrhotite, mackinawite, etc ...) strongly absorb the red laser radiation, thermal effects are easily caused by the increasing temperature on the measuring spot. In order to show the changes induced by the laser power in mackinawite signal, a
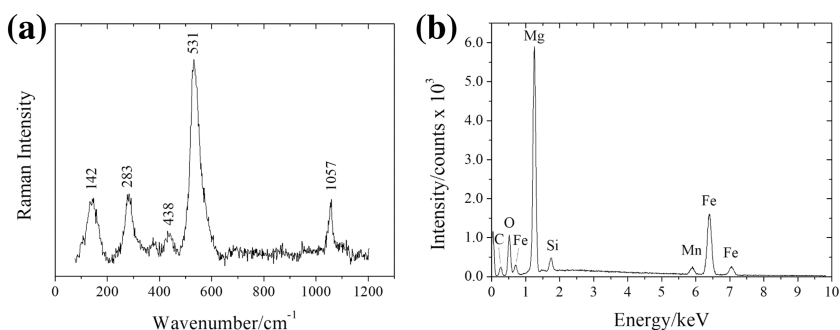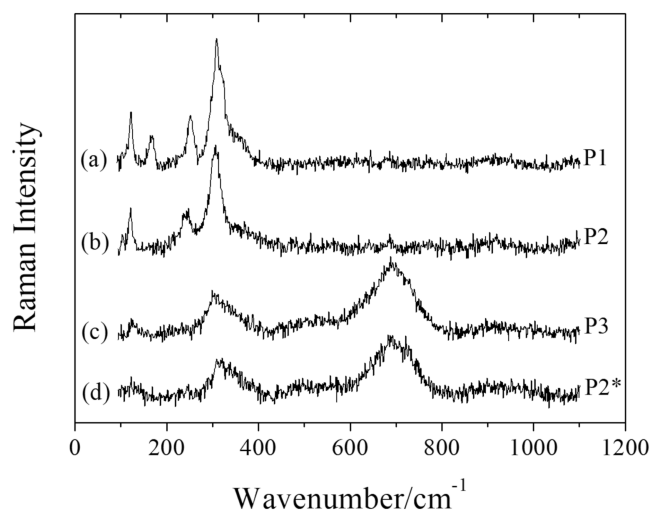
FIGURE 5 (a) Raman spectrum and (b) energy dispersive system (EDS) spectrum on an Fe-Mg carbonate crystal in Balangero chrysotile.

FIGURE 7 Raman spectra on a partially oxidized mackinawite crystal in Balangero chrysotile obtained at 632.8 nm at different laser powers with P1 < P2 < P3: (a) acquisition at P1; (b) acquisition at P2; (c) acquisition at P3; (d) acquisition at P2 obtained after that at P3, lowering the power.

FIGURE 6 (a) Scanning electron microscope secondary electron image (SEM-SEI) of a mackinawite crystal in Balangero chrysotile, highlighted by the yellow arrow; (b) Raman spectra acquired on Fe sulfides in Balangero chrysotile as (I) nanocrystalline mackinawite, (II) partially oxidized mackinawite, (III) nanocrystalline and partially oxidized mackinawite, and (IV) Fe-Ni sulfide. Nanocrystalline mackinawite features are marked with the symbol §; partially oxidized mackinawite features are marked with the symbol ◇; Fe-Mg carbonate feature mixed with sulfide signals is marked with an asterisk (*). [Colour figure can be viewed at wileyonlinelibrary. com]

crystal of partially oxidized mackinawite was chosen in the sample, and its Raman spectrum was obtained at different laser powers: 0.08 mW (P1), 0.32 mW (P2), and 0.80 mW (P3). The Raman spectra were acquired at increasing power from P1 to P3, on the same measuring point. Then, the laser power was lowered to P2, in order to evaluate the reversibility of the transformation through the spectral changes. The results are shown in Figure 7.

At the lowest laser power, the Raman spectrum of partially oxidized mackinawite was obtained (Figure 7a). Increasing the laser power from P1 to P2, Raman peaks broadened and shifted towards lower wavenumbers (Figure 7b). The main signal at 309 cm^{-1} and the shoulder at 323 cm^{-1} were no longer observed, and one band only occurred at ∼306 cm^{-1}. The feature at 253 cm^{-1} was shifted to 241 cm^{-1}, and a peak broadening (full width at half maximum [FWHM]) was observed from 18 to 35 cm^{-1}. The peak at 122 cm^{-1} was shifted to 120 cm^{-1}, whereas the contribution at 168 cm^{-1} disappeared. This thermal shift induced by the increasing laser power was recovered lowering to the initial value (data not shown). When the laser power raised from P2 to P3, the contribution at ∼300 cm^{-1} broadened with a FWHM from ∼30 cm^{-1} (at lower power) to ∼75 cm^{-1}, and a new intense broad band (FWHM ∼110 cm^{-1}) was observed at ∼690 cm^{-1} (Figure 7c). Lowering the laser power from P3 to P2 (marked as P2* in Figure 7d) suggests that the transformation induced in this range is irreversible: the Raman spectrum resembles that acquired at P3, without recovering the characteristics obtained at P2. The broad and intense band at ∼690 cm^{-1} still occurred at P2*. In addition, the features at ∼300 cm^{-1} exhibited a small upshift (∼15 cm^{-1}) from P3 to P2*, showing the effect of a thermal shift. It is important to highlight that the sensitivity to the laser power depends on the surface morphology of the mackinawite crystals. Some spots were considerably less stable under higher laser powers. P1, P2, and P3 were reported as relative references, but usually, similar peak broadening and shifts were observed at

different laser powers. The formation of new bands at higher power was also recorded at variable powers, suggesting that the threshold power to induce irreversible changes depends on the stability of the crystal.

Overall, the micrometric Fe-bearing impurities found in Balangero chrysotile by Raman and SEM-EDS analyses are summarized in Table 1. A comparison of the minor phases detected here and in the work of Pollastri and coworkers[25] is also reported in Table 1. The investigation with micro-Raman spectroscopy enabled the identification of these impurities also at trace level, whose occurrence is under the detection limit of other analytical techniques (e.g. X-ray powder diffractometry).

Though the detected Fe-bearing compounds are minor phases in Balangero chrysotile, they might potentially contribute to the toxicity, if they dissolve in the macrophage acidic environment (pH ~ 4–5). Fe oxides and oxyhydroxides are scarcely soluble, except at extreme pH values.[72] *In vitro* studies reported no or low toxicity for Fe_3O_4 and Fe_2O_3.[73,74] Differently, the dissolution of Fe sulfides was observed in acidic environment. Jeong and coworkers[75] proved that at pH 4.9 mackinawite dissolved after a few hours. Following a non-oxidative dissolution, most of the structural Fe(II) is released into the solution without being oxidized.[75] The dissolved Fe sulfides in the organic environment might be considered—though, as of today, *in vitro* studies about the toxicity of mackinawite were not reported—as a carrier of toxic metals (i.e., Fe(II)), inducing the so-called "Trojan horse effect." This mechanism was observed for a range of metal-containing nanoparticles, with the intracellular release of toxic metal ions triggered by the acidic environment of the lysosomes. Acute inflammatory effects—

including ROS production, oxidative stress, and DNA damage—were induced by the released metals.[7,76]

4 | CONCLUSIONS

Raw chrysotile from the Balangero mine (Italy) contains a number of mineralogical species other than chrysotile fibers. One of the mechanisms invoked to explain the toxicity of chrysotile involves the release of Fe—and other redox active metals—during dissolution processes occurring within lung tissue. Given the heterogeneous nature of Balangero chrysotile, it is critical to detect the presence of Fe-bearing impurities that could potentially become additional pools of available Fe. Through micro-Raman spectroscopy, combined with SEM-EDS analysis, the mineralogical characterization of Balangero chrysotile was obtained, focusing on the fibrous phases and the Fe compounds. Chrysotile, the main fibrous phase, shows the typical morphology of curvilinear bundle of fibers with frayed ends. Raman analysis of chrysotile fibers proved the presence of Cr^{3+} through its characteristic luminescence bands. Cr is known to be found as trace metal, substituting Mg in the octahedral sites of brucite layer. In addition to chrysotile fibers, plate lamellae of antigorite and rigid fibers of balangeroite were found and distinguished by their characteristic Raman spectra, both in the low-wavenumber and in the OH-stretching spectral regions, thanks to the use of different laser wavelengths. It is worth noting the presence of Fe as a structural element in balangeroite fibers.

Furthermore, Fe-bearing impurities were identified in micro-crystals, ranging from few micrometers to ~40 μm, being located near and on the surface of the fibers. As often reported for chrysotile asbestos, the most abundant Fe compound is magnetite. In addition to that, the rarer presence of Fe oxides and oxyhydroxides as ilmenite, hematite, and lepidocrocite was assessed by the micro-Raman characterization. Fe-bearing compounds are not restricted to oxides and oxyhydroxides as Fe sulfides were detected as well. Different forms of mackinawite Fe(II)S were distinguished by their characteristic Raman signals and by the presence of Fe and S in the EDS spectra, consisting of nanocrystalline mackinawite and partially oxidized mackinawite $(Fe(II)_{1-3x}Fe(III)_{2x}S)$. It is noteworthy that the occurrence of these Fe sulfides is uncommonly reported as associated minerals in chrysotile asbestos. Occasionally, Fe-Ni sulfide and Mg-Fe carbonate impurities were also found, although the mineral phases were not precisely identified.

To conclude, the combination of micro-Raman spectroscopy and SEM-EDS analysis proved to be effective for characterizing Balangero chrysotile at the micro-scale, highlighting both the presence of fibrous mineral phases

TABLE 1 Minor phases detected in Balangero chrysotile. The analytical techniques used for the identification are reported.

Micro-Raman spectroscopy	X-ray powder diffraction
This work (Fe-bearing compounds)	Pollastri et al.[25]
Antigorite	Antigorite
Balangeroite	Balangeroite
Fe-Mg carbonate	Calcite
Fe-Ni sulfide	Clinochlore
Hematite	Diopside
Ilmenite	Dolomite
Lepidocrocite	Magnetite
Mackinawite	Microcline
Magnetite	Plagioclase
	Talc

and micrometric Fe compounds. Toxic metals, such as Cr and Ni detected in the fibers and in non-fibrous species, should be considered as possible sources of metal release when the fibers are dissolved in the organic environment. Furthermore, the presence of Fe(II) and Fe(III) species is remarked here, both as structural element of the fibers—in balangeroite—and as minor component—in Fe compounds. The dissolution of Fe-bearing compounds, such as mackinawite, with the "Trojan horse" mechanism in acidic environment, might be taken into consideration in the investigation of the acute effects induced by Balangero chrysotile. These findings are expected to be helpful in ongoing and future toxicological studies aimed at understanding pathogenic mechanisms of asbestos.

DATA AVAILABILITY STATEMENT

The data that support the findings of this study are available from the corresponding author upon reasonable request.

ORCID

Laura Fornasini https://orcid.org/0000-0002-6794-0828
Simona Raneri https://orcid.org/0000-0002-3135-7083
Luciana Mantovani https://orcid.org/0000-0001-7438-1887

REFERENCES

[1] IARC Working Group on the Evaluation of Carcinogenic Risks to Humans and others, *Arsenic, metals, Fibres and dusts*, Vol. 100, IARC Press, International Agency for Research on Cancer, Lyon, France **2012**.

[2] A. F. Gualtieri, *Mineral Fibres: Crystal Chemistry, Chemical-Physical Properties, Biological Interaction and Toxicity*, European Mineralogical Union and the Mineralogical Society of Great Britain, London **2017**.

[3] J. E. Alleman, B. T. Mossman, *Sci. Am.* **1997**, *277*, 70.

[4] A. F. Gualtieri, in *Toxicity of Building Materials*, (Eds: F. Pacheco-Torgal, S. Jalali, A. Fucic), Woodhead Publishing, Sawston, Cambridge, UK **2012**, 166.

[5] International Ban Asbestos Secretariat. - *Current Asbestos Bans*, http://www.ibasecretariat.org/alpha_ban_list.php (accessed 18 February 2022).

[6] A. F. Gualtieri, M. Lassinantti Gualtieri, V. Scognamiglio, D. di Giuseppe, in *Ecological and Health Effects of Building Materials*, (Eds: J. A. Malik, S. Marathe), Springer, Switzerland **2022**, 297.

[7] A. F. Gualtieri, G. Lusvardi, A. Zoboli, D. di Giuseppe, M. Lassinantti Gualtieri, *Environ. Res.* **2019**, *171*, 550.

[8] J. A. Hardy, A. E. Aust, *Chem. Rev.* **1995**, *95*, 97.

[9] B. Fubini, L. Mollo, *Toxicol. Lett.* **1995**, *82–83*, 951.

[10] E. Gazzano, E. Foresti, I. G. Lesci, M. Tomatis, C. Riganti, B. Fubini, N. Roveri, D. Ghigo, *Toxicol. Appl. Pharmacol.* **2005**, *206*, 356.

[11] E. Gazzano, F. Turci, E. Foresti, M. G. Putzu, E. Aldieri, F. Silvagno, I. G. Lesci, M. Tomatis, C. Riganti, C. Romano, B. Fubini, N. Roveri, D. Ghigo, *Chem. Res. Toxicol.* **2007**, *20*, 380.

[12] L. Pascolo, A. Gianoncelli, B. Kaulich, C. Rizzardi, M. Schneider, C. Bottin, M. Polentarutti, M. Kiskinova, A. Longoni, M. Melato, *Part. Fibre Toxicol.* **2011**, *8*, 7.

[13] L. Pascolo, A. Gianoncelli, G. Schneider, M. Salomé, M. Schneider, C. Calligaro, M. Kiskinova, M. Melato, C. Rizzardi, *Sci. Rep.* **2013**, *3*, 1.

[14] S. Pollastri, A. F. Gualtieri, R. Vigliaturo, K. Ignatyev, E. Strafella, A. Pugnaloni, A. Croce, *Chemosphere* **2016**, *164*, 547.

[15] D. di Giuseppe, A. Zoboli, R. Vigliaturo, R. Gieré, M. P. Bonasoni, O. Sala, A. F. Gualtieri, *Minerals* **2019**, *9*, 618.

[16] F. J. Wicks, D. S. O'Hanley, *Rev. Mineral. Geochemistry* **1988**, *19*, 91.

[17] P. Ballirano, A. Bloise, A. F. Gualtieri, M. Lezzerini, A. Pacella, N. Perchiazzi, M. Dogan, A. U. Dogan, *Mineral Fibers: Crystal Chemistry, Chemical-Physical Properties, Biological Interaction and Toxicity*, Vol. 18, European Mineralogical Union and the Mineralogical Society of Great Britain, Twickenham, UK **2017**, 17.

[18] G. Stroink, C. Blaauw, C. G. White, W. Leiper, *Can. Mineral.* **1980**, *18*, 285.

[19] C. Blaauw, G. Stroink, W. Leiper, *Can. Mineral.* **1979**, *17*, 713.

[20] A. Bloise, D. Barca, A. F. Gualtieri, S. Pollastri, E. Belluso, *Environ. Pollut.* **2016**, *216*, 314.

[21] J. S. Harington, F. J. C. Roe, *Ann. N. Y. Acad. Sci.* **1965**, *132*, 439.

[22] J. R. Dixon, D. B. Lowe, D. E. Richards, L. J. Cralley, H. E. Stokinger, *Cancer Res.* **1970**, *30*, 1068.

[23] A. Holmes, A. Morgan, F. J. Sandalls, *Am. Ind. Hyg. Assoc. J.* **1971**, *32*, 281.

[24] A. Morgan, A. E. Lally, A. Holmes, *Ann. Occup. Hyg.* **1973**, *16*, 231.

[25] S. Pollastri, N. Perchiazzi, M. Lezzerini, J. R. Plaisier, A. Cavallo, M. C. Dalconi, N. B. Gandolfi, A. F. Gualtieri, *Period. di Mineral.* **2016**, *85*, 249.

[26] C. Groppo, R. Compagnoni, *Period. di Mineral.* **2007**, *76*, 127.

[27] P. Rossetti, S. Zucchetti, *Rend. della Soc. Ital. di Mineral. E Petrol.* **1988**, *43*, 139.

[28] S. Zucchetti, *Geoing. Ambient. E Mineraria* **1968**, *5*, 106.

[29] R. L. Virta, *Mineral Commodity Profiles—Asbestos*, US Geological Survey Reston, VA **2005**.

[30] *Gazzetta Ufficiale n. 116 21-05-1990*, Serie Generale, **1990**, p. 17, https://www.gazzettaufficiale.it/eli/gu/1990/05/21/116/sg/pdf

[31] F. Turci, S. E. Favero-Longo, C. Gazzano, M. Tomatis, L. Gentile, M. Bergamini, *J. Hazard. Mater.* **2016**, *308*, 321.

[32] C. Avataneo, E. Belluso, S. Capella, D. Cocca, M. Lasagna, G. Pigozzi, D. A. D. E. Luca, *Ital. J. Eng. Geol. Environ.* **2021**, *1*, 5.

[33] C. Avataneo, J. R. Petriglieri, S. Capella, M. Tomatis, M. Luiso, G. Marangoni, E. Lazzari, S. Tinazzi, M. Lasagna, D. A. de Luca, M. Bergamini, E. Belluso, F. Turci, *J. Hazard. Mater.* **2022**, *424*, 127528.

[34] A. F. Gualtieri, S. Pollastri, N. Bursi Gandolfi, M. L. Gualtieri, *Sci. Rep.* **2018**, *8*, 1.

[35] A. F. Gualtieri, G. Lusvardi, A. Pedone, D. di Giuseppe, A. Zoboli, A. Mucci, A. Zambon, M. Filaferro, G. Vitale, M. Benassi, R. Avallone, L. Pasquali, M. Lassinantti Gualtieri, *Chem. Res. Toxicol.* **2019**, *32*, 2063.

[36] D. di Giuseppe, S. Scarfì, A. Alessandrini, A. M. Bassi, S. Mirata, V. Almonti, G. Ragazzini, A. Mescola, M. Filaferro, R. Avallone, G. Vitale, V. Scognamiglio, A. F. Gualtieri, *Toxicology* **2022**, *466*, 153081.

[37] E. Belluso, A. Cavallo, D. Halterman, *Mineral Fibers: Crystal Chemistry, Chemical-Physical Properties, Biological Interaction and Toxicity* Vol. 18, European Mineralogical Union and the Mineralogical Society of Great Britain, Twickenham, UK **2017**, 65.

[38] E. Belluso, A. Baronnet, S. Capella, *Environ. Eng. Geosci.* **2020**, *26*, 39.

[39] S. Pollastri, F. D'Acapito, A. Trapananti, I. Colantoni, G. B. Andreozzi, A. F. Gualtieri, *J. Hazard. Mater.* **2015**, *298*, 282.

[40] R. Compagnoni, G. Ferraris, L. Fiora, *Am. Mineral.* **1983**, *68*, 214.

[41] M. Mellini, *Mineral. Mag.* **1986**, *50*, 301.

[42] C. Groppo, M. Tomatis, F. Turci, E. Gazzano, D. Ghigo, R. Compagnoni, B. Fubini, *J. Toxicol. Environ. Heal. - Part A* **2005**, *68*, 1.

[43] F. Turci, M. Tomatis, R. Compagnoni, B. Fubini, *Ann. Occup. Hyg.* **2009**, *53*, 491.

[44] S. Mirata, V. Almonti, D. di Giuseppe, L. Fornasini, S. Raneri, S. Vernazza, D. Bersani, A. F. Gualtieri, A. M. Bassi, S. Scarfì, *Int. J. Mol. Sci.* **2022**, *23*, 2840.

[45] J. R. Petriglieri, E. Salvioli-Mariani, L. Mantovani, M. Tribaudino, P. P. Lottici, C. Laporte-Magoni, D. Bersani, *J. Raman Spectrosc.* **2015**, *46*, 953.

[46] C. Rinaudo, D. Gastaldi, E. Belluso, *Can. Mineral.* **2003**, *41*, 883.

[47] A. Croce, A. Arrais, C. Rinaudo, *Minerals* **2018**, *8*, 249.

[48] C. Groppo, C. Rinaudo, S. Cairo, D. Gastaldi, R. Compagnoni, *Eur. J. Mineral.* **2006**, *18*, 319.

[49] R. Compagnoni, R. Cossio, M. Mellini, *J. Raman Spectrosc.* **2021**, *52*, 1334.

[50] C. Rinaudo, A. Croce, *Appl. Sci.* **2019**, *9*, 3092.

[51] M. Gaft, R. Reisfeld, G. Panczer, *Modern Luminescence Spectroscopy of Minerals and Materials*, Springer, Berlin, Heidelberg, Germany **2015**.

[52] V. I. Solomonov, A. V. Spirina, M. P. Popov, A. S. Makarova, A. G. Nikolaev, A. N. Orlov, *J. Opt. Technol.* **2021**, *88*, 610.

[53] J. S. Harington, *Ann. N. Y. Acad. Sci.* **1965**, *132*, 31.

[54] A. L. Auzende, I. Daniel, B. Reynard, C. Lemaire, F. Guyot, *Phys. Chem. Miner.* **2004**, *31*, 269.

[55] D. R. Veblen, P. R. Buseck, *Science (80-.)* **1979**, *206*, 1398.

[56] J. R. Petriglieri, C. Laporte-Magoni, E. Salvioli-Mariani, M. Tomatis, E. Gazzano, F. Turci, A. Cavallo, B. Fubini, *Environ. Eng. Geosci.* **2020**, *26*, 89.

[57] J. R. Petriglieri, D. Bersani, C. Laporte-Magoni, M. Tribaudino, A. Cavallo, E. Salvioli-Mariani, F. Turci, *Appl. Sci.* **2021**, *11*, 287.

[58] E. Belluso, G. Ferraris, *Eur. J. Mineral.* **1991**, *3*, 559.

[59] R. Compagnoni, G. Ferraris, M. Mellini, *Am. Mineral.* **1985**, *70*, 767.

[60] E. Belluso, E. Fornero, S. Cairo, G. Albertazzi, C. Rinaudo, *Can. Mineral.* **2007**, *45*, 1495.

[61] D. Bersani, P. P. Lottici, A. Montenero, *J. Raman Spectrosc.* **1999**, *30*, 355.

[62] D. L. A. de Faria, S. Venâncio Silva, M. T. de Oliveira, *J. Raman Spectrosc.* **1997**, *28*, 873.

[63] F. J. Wicks, E. J. W. Whittaker, *Can. Mineral.* **1977**, *15*, 459.

[64] A. Wang, K. E. Kuebler, B. L. Jolliff, L. A. Haskin, *Am. Mineral.* **2004**, *89*, 665.

[65] H. N. Rutt, J. H. Nicola, *J. Phys. C Solid State Phys.* **1974**, *7*, 4522.

[66] E. S. Zhitova, I. V. Pekov, N. V. Chukanov, V. O. Yapaskurt, V. N. Bocharov, *Russ. Geol. Geophys.* **2020**, *61*, 36.

[67] E. S. Zhitova, G. Y. Ivanyuk, S. V. Krivovichev, V. N. Yakovenchuk, Y. A. Pakhomovsky, Y. A. Mikhailova, *Geol. Ore Depos.* **2017**, *59*, 652.

[68] E. B. Hansson, M. S. Odziemkowski, R. W. Gillham, *Corros. Sci.* **2006**, *48*, 3767.

[69] J. A. Bourdoiseau, M. Jeannin, R. Sabot, C. Rémazeilles, P. Refait, *Corros. Sci.* **2008**, *50*, 3247.

[70] J. A. Bourdoiseau, M. Jeannin, C. Rémazeilles, R. Sabot, P. Refait, *J. Raman Spectrosc.* **2011**, *42*, 496.

[71] S. Boursiquot, M. Mullet, M. Abdelmoula, J. M. Génin, J. J. Ehrhardt, *Phys. Chem. Miner.* **2001**, *28*, 600.

[72] R. M. Cornell, U. Schwertmann, *The Iron Oxides: Structure, Properties, Reactions, Occurrences and Uses*, John Wiley & Sons, Weinheim, Germany **2003**.

[73] S. M. Hussain, K. L. Hess, J. M. Gearhart, K. T. Geiss, J. J. Schlager, *Toxicol. In Vitro* **2005**, *19*, 975.

[74] H. L. Karlsson, P. Cronholm, J. Gustafsson, L. Möller, *Chem. Res. Toxicol.* **2008**, *21*, 1726.

[75] H. Y. Jeong, Y. S. Han, S. W. Park, K. F. Hayes, *Geochim. Cosmochim. Acta* **2010**, *74*, 3182.

[76] S. Sabella, R. P. Carney, V. Brunetti, M. A. Malvindi, N. Al-Juffali, G. Vecchio, S. M. Janes, O. M. Bakr, R. Cingolani, F. Stellacci, P. P. Pompa, *Nanoscale* **2014**, *6*, 7052.

SUPPORTING INFORMATION

Additional supporting information can be found online in the Supporting Information section at the end of this article.